Sensitivity of Localized Surface Plasmon Resonance and Acoustic Vibrations to Edge Rounding in Silver Nanocubes

Charles Vernier, Lucien Saviot, Yinan Fan, Alexa Courty, Hervé Portalès

Sensitivity of Localized Surface Plasmon Resonance and Acoustic Vibrations to Edge Rounding in Silver Nanocubes

Charles Vernier,[†] Lucien Saviot,[*,‡] Yinan Fan,[†] Alexa Courty,[†] and Hervé Portalès[*,†]

[†]*Sorbonne Université, CNRS, MONARIS, UMR 8233, 75005 Paris, France*

[‡]*Laboratoire Interdisciplinaire Carnot de Bourgogne, UMR 6303 CNRS-Université Bourgogne Franche-Comté, 21078 Dijon, Cedex, France*

E-mail: lucien.saviot@u-bourgogne.fr; herve.portales@sorbonne-universite.fr

Abstract

Precise knowledge of the dependence of nano-object properties on their structural characteristics such as their size, shape, composition or crystallinity, in turn enables them to be finely characterized using appropriate techniques. Spectrophotometry and inelastic light scattering spectroscopy are non-invasive techniques that are proving highly robust and efficient for characterizing the optical response and vibrational properties of metal nano-objects. Here, we investigate the optical and vibrational properties of monodomain silver nanocubes synthesized by chemical route, with edge length ranging from around 20 to 58 nm. The synthesized nanocrystals are not perfectly cubic and exhibit rounded edges and corners. This rounding was quantitatively taken into account by assimilating the shape of the nanocubes to superellipsoids. The effect of rounding on their optical response was clearly evidenced by localized surface plasmon resonance

spectroscopy and supported by calculations based on the discrete dipole approximation method. The study of their acoustic vibrations by high-resolution low-frequency Raman scattering revealed a substructure of the T_{2g} band, which was analyzed as a function of rounding. The measured frequencies are consistent with the existence of an anticrossing pattern of two T_{2g} branches. Such an avoided crossing in the T_{2g} modes is clearly evidenced by calculating the vibrational frequencies of silver nanocubes using the Rayleigh-Ritz variational method that accounts for both their real size, shape and cubic elasticity. These results show that it is possible to assess the rounding of nanocubes, including by means of ensemble spectroscopic measurements on well-calibrated particles.

Abbreviations

NCB,TEM,LFRS,LSPR,DDA,RR,FWHM

Keywords

monodomain nanocrystals, resonant Raman scattering, superellipsoid, discrete-dipole approximation, Rayleigh-Ritz variational method

The localized surface plasmon resonance (LSPR) of metal nano-objects is a feature well-known to be sensitive to many factors such as their size, shape, composition, environment and interaction with neighboring nanoparticles.[1–4] In the last decades, continuing progress in the synthesis of noble metal nanoparticles with controlled morphologies, in particular *via* colloidal routes,[5] enabled to take advantage of such morphology-dependent properties for applications in various fields including, for instance, biosensing,[6] photothermal heating,[7] and surface-enhanced Raman spectroscopy.[8,9] It turns out that the dependence of the properties of nano-objects on their characteristics can also be used as a tool for characterizing them. This approach, based on comparing their measured and computed responses, has already

been applied on ensembles and single nano-objects by studying their optical absorption and scattering spectra.[1,10–12] Similarly, the acoustic vibrations of nano-objects depend strongly on their size,[13–15] shape,[16–18] composition,[19–22] and environment.[23–26] In addition, investigating the vibrational properties of nanoparticles can yield additional information such as the size dispersion of the nano-objects,[27] their elasticity,[20,28,29] their crystalline structure,[30–33] and the mechanical coupling with their environment.[23,34] The use of vibrations to investigate the mechanical coupling between nanoparticles in systems such as dimers[35–38] or compact assemblies of nanoparticles,[39,40] as well as the contact at the metal-dielectric interface in core-shell nanoparticles,[22,41] has already proved highly successful. Non-contact spectrally[42] or temporally[25,43] resolved optical techniques are well suited for studying the vibrations of matrix-embedded or deposited noble metal nano-objects by taking advantage of their LSPR. Time-resolved pump-probe spectroscopy probes the modulation of the LSPR frequency in nano-objects induced by the acoustic vibrations that are optically launched.[44,45] This technique mainly enables the detection of totally symmetric acoustic modes such as the breathing mode. On the other hand, low-frequency Raman scattering (LFRS) experiments on nano-objects allow detecting different vibrational modes, including non-totally symmetric ones.[46] This other spectroscopic technique is based on the modulation of scattering efficiency resulting from the periodic polarizability changes the vibrations induce.[47] In addition, the inelastic light scattering process involved in metallic nano-objects benefits from various coupling mechanisms between the surface plasmon-polaritons and the confined vibrations within the nano-objects resulting in an exaltation of the plasmon-assisted Raman scattering under resonant excitation.[32,48–52] These techniques are therefore complementary and powerful tools to address the vibrational properties of plasmonic nano-objects.

As mentioned above, a large variety of noble metal nanoparticles differing by their morphology, composition and internal structure have been characterized by using these techniques, either in ensemble or single-particle measurements. Among them, metal nanocubes (NCBs) have recently attracted a great deal of interest as promising candidates for applica-

tions in plasmonics, nanocatalysis and nanophotonics.[33,53–56] In most cases, it appears that corners are rounded at the nanoscale,[57] prompting a huge synthesis effort aimed at obtaining NCBs with the desired size and shape while precisely controlling their corner sharpness.[53,58] Indeed, as some works dealing with NCBs have already shown, the edge rounding can play a decisive role by modifying their properties and significantly impact their effectiveness for applications.[3,55,59–62] Measurements on single objects or dimers deposited on a substrate are commonly used to correlate the properties of nano-objects with their morphology.[12,60,63] This aims to avoid the recorded signal being obscured by the inhomogeneous broadening effect that occurs in ensemble-averaged measurements.[11] However, unknown interactions between the nanoparticles and the substrate, as well as the need for perfect knowledge of the individual morphology of the nano-objects being studied often make it difficult to interpret the results of such experiments.[63] Ensemble measurements are suitable to overcome this difficulty provided very well calibrated nano-objects can be synthesized.[24,53] So far, only a few works have been published on the study of confined eigenvibrations of NCBs, by using spectrocopy techniques, either in the time[64,65] or frequency domains.[63,66,67] Such a lack of data and the failure, in most cases, to take into account the anisotropic elasticity of the materials, make it not possible to verify experimentally the effect of rounding on the vibrational frequencies, as expected from recent calculations.[68]

In this work, we report highlights on very low frequency acoustic vibrations of Ag NCBs chemically synthesized with very narrow size and morphology (edge rounding) dispersions, as precisely determined by transmission electron microscopy analysis. The sensitivity of their optical response to the rounding is established through extinction measurements performed on colloidal solutions, and is also supported by electrodynamics calculations based on the Discrete Dipole Approximation (DDA) method. The acoustic vibrations of Ag NCBs are investigated by low-frequency Raman scattering (LFRS), with a high level of resolution for such ensemble measurements. This allows addressing accurately the impact of edge rounding of NCBs on their acoustic modes, as well as comparing the vibrational frequencies measured

experimentally with those calculated by taking into account both the NCB size, shape and cubic elasticity.

Results and discussion

Various batches of monodomain Ag NCBs were synthesized using the chemicals and protocols[69,70] described in the METHODS section. The NCBs issued from these batches have different edge lengths and roundings. As mentioned above, this work goes far beyond controlling the size of Ag NCBs. It aims at precisely characterizing the impact of the edge rounding on both the LSPR and acoustic vibrations. Indeed, so-called NCBs are not perfect cubes but actually exhibit rounded edges and corners which can not be ignored due to their small sizes, as shown in Figure 1A. To quantify such a rounding, the studied Ag NCBs are modeled by superellipsoids whose surface is defined by the implicit equation:

$$\left|\frac{x}{a}\right|^r + \left|\frac{y}{a}\right|^r + \left|\frac{z}{a}\right|^r = 1 \tag{1}$$

where a is the half-length along the x, y and z axes, and $r > 0$ controls the rounding of the shape edges. We introduce the parameter $e = 2a$ as being the edge length of the cube in which the superellipsoid is inscribed. r will be referred to as the rounding parameter in the following. Indeed, it provides a quantitative assessment of the edge and corner rounding characterizing each batch of Ag NCBs. The shape evolves from that of a sphere ($r = 2$) to the one of a perfect cube at the limit $r \to \infty$ (see Figure S1 in SI). Progressively increasing the r-value, from the former to the latter of these two cases, leads to shapes that reproduce well rounded cubes with sharper and sharper edges and corners. Assimilating the synthesized NCBs to superellipsoids allows to satisfactorily model their shape. This will be very helpful when calculating their extinction coefficient or vibrational frequencies while properly accounting for their rounding. Cross-sections of the superellipsoids along the xy, yz or zx planes are superellipses related to the same r-value. They correspond to the

external shape as seen in a top view as in TEM images. As an example, Figure 1B shows a superellipse with rounding parameter $r = 3.6$. In the following, each sample will be named NCB(r), replacing r by the mean rounding parameter determined for the corresponding batch of Ag NCBs.

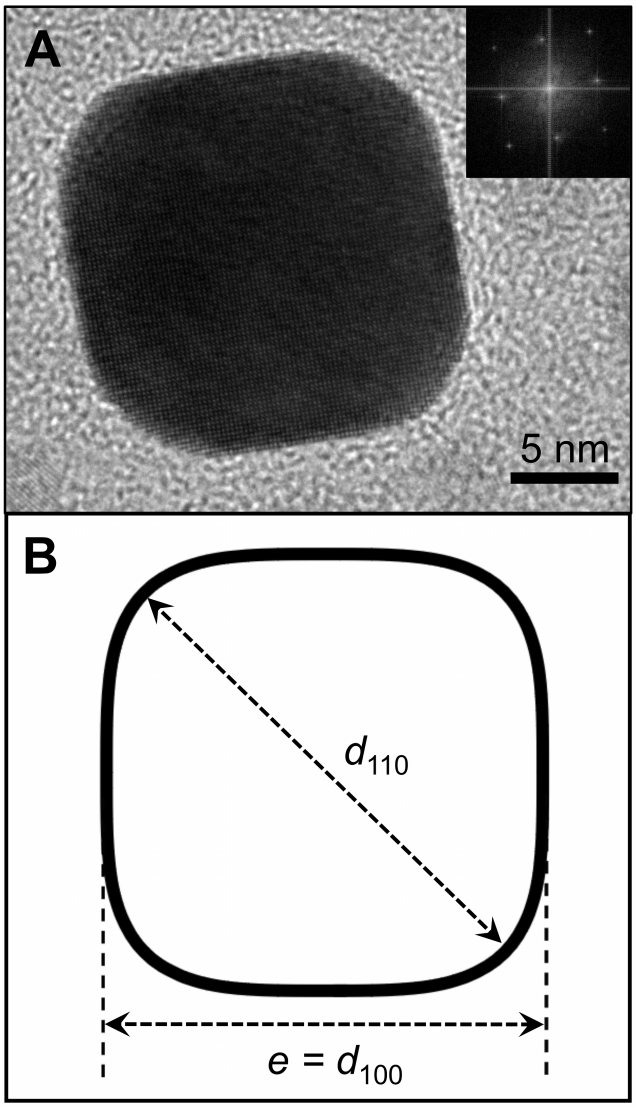

Figure 1: **HRTEM observation and modeling the cross section of the NCBs.** (A) HRTEM image and power spectrum of one single Ag NCB issued from sample NCB(3.6). (B) Superellipse profile related to $r = 3.6$, as determined from the ratio of the d_{110} by d_{100} lengths.

Together with the r-value of the rounding parameter, each NCB is also characterized by its size identified here as being the length e aforementioned. The high-resolution trans-

mission electron microscopy (HRTEM) image of one single Ag NCB presented in Figure 1A reveals its monodomain structure, which is terminated by {100} facets, as illustrated by the power spectrum shown in the inset of Figure 1A. From that observation, the mean r-value characterizing each batch of NCBs was assessed thanks to the d_{110}/d_{100} ratio calculated from at least 50 NCBs, where d_{110} and $d_{100}(= e)$ are the lengths of the nanocrystal along the $\langle 110 \rangle$ and $\langle 100 \rangle$ directions (Figure S2). TEM images of Ag NCBs issued from the various samples are shown in Figure 2 along with the corresponding size histograms. The mean values of both the NCB size and rounding parameter estimated for each sample are given in Table 1. The increase in both e and r observed for samples NCB(3.6), NCB(4.7), and NCB(7.7), which were prepared using the same protocol, indicates that these two parameters are not independent for these three samples, *i.e.* the larger the NCBs, the sharper their edges. However, it should be noted that in terms of shape, NCB rounding is not correlated with an increase in their radius of curvature, r_c. To illustrate this, the radii of curvature of the NCBs were calculated and their values reported in Table 1. With the exception of the most rounded NCBs from sample NCB(2.8), which have a significantly larger radius of curvature than the others, the NCBs from the other three samples exhibit similar radii of curvature.

Table 1: NCB size, e, radius of curvature, r_c, and rounding parameter, r, as derived from TEM analysis and calculation of the d_{110}/d_{100} ratio. The characteristic size, $V^{\frac{1}{3}}$, related to each sample is also provided.

sample	e (nm)	r_c (nm)	r	$V^{\frac{1}{3}}$ (nm)
NCB(2.8)	26.0 ± 3.1	8.0 ± 2.5	2.8 ± 0.3	22.9
NCB(3.6)	20.3 ± 1.9	4.6 ± 1.5	3.6 ± 0.5	18.7
NCB(4.7)	35.5 ± 2.5	5.9 ± 1.7	4.7 ± 0.7	33.7
NCB(7.7)	58.0 ± 4.8	5.6 ± 2.0	7.7 ± 1.6	56.7

Localized surface plasmon resonance

Extinction spectra of the colloidal solutions were recorded using a Varian 50 Scan spectrophotometer after two washing steps. The measured extinction spectra are shown in Fig-

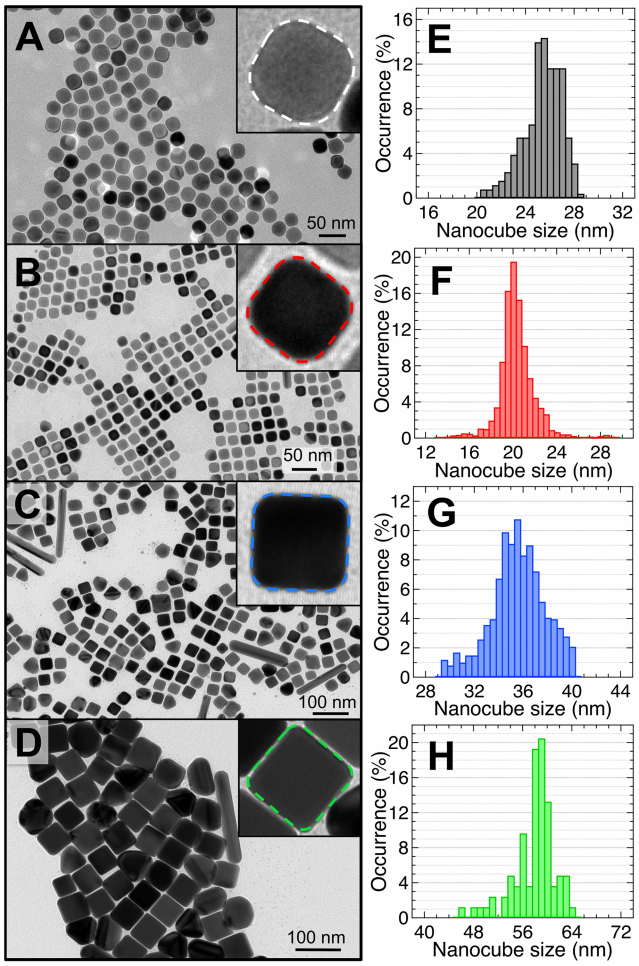

Figure 2: **TEM images and size histograms of Ag NCBs.** Typical TEM images of NCBs issued from the various samples are shown: (A) NCB(2.8), (B) NCB(3.6), (C) NCB(4.7), and (D) NCB(7.7). Each inset shows a zoom of one single NCB outlined with a superellipse whose profile is designed from the sample related r-value. The size histograms (E)–(H) are plotted next to the corresponding TEM image.

ure 3A–D. Each spectrum is dominated by an absorption band corresponding to the LSPR of the NCBs. While an electric dipolar plasmon mode is responsible for the major contribution to the spectrum, weaker bands and shoulders observed at lower wavelengths originate from higher-order plasmonic modes. These additional bands are due to quadrupole and octupole plasmon resonances localized at the corner and edges of the NCBs.[71] As already reported in the literature[3,4,55] and as will be confirmed below through numerical simulations, these additional plasmon modes are characteristic of cubic nanoparticles. Hence, observation of these bands in the extinction spectrum of nanoparticles dispersed in aqueous solution may confirm they are cubic in shape. Such a correlation has been previously experienced for NCBs with similar structural features and optical spectra than those studied here.[55] No quadrupolar or octupolar modes is visible on the low wavelength side of the LSPR band in sample NCB(2.8) (Figure 3A). The difficulty to discern them in that sample may be due to the fact that the NCBs have the lowest rounding parameter or, equivalently, the roundest edges and corners. From Figure 3B–D, it is straightforward to note that the position of the LSPR band maximum changes from one sample to the other, redshifting significantly for increasing size and rounding parameter. More specifically, it is centered on wavelengths of $\lambda_{\mathrm{LSPR}} = 405$, 428 and 465 nm for samples NCB(3.6), NCB(4.7) and NCB(7.7), in order of increasing e and r values (Table 1). For sample NCB(2.8), toluene was used as solvent to redisperse the NCBs whereas water was used for the three other samples. As the refractive indices of these two solvents are different, the wavelength at the band maximum measured in sample NCB(2.8), *i.e.* $\lambda_{\mathrm{LSPR}} = 417$ nm, cannot be directly compared with the others.

In contrast with the main LSPR band behavior, it should be noted that the wavelength of the other plasmon modes do not exhibit any clear dependence on size nor rounding parameter. This shows that the dipolar mode is much more sensitive to changes in edge and corner rounding than higher-order plasmonic modes. It should be noted that similar results have already been reported in the case of single Ag NCBs in the vicinity of a dielectric substrate.[60] However, the presence of the substrate and the strong difference in dielectric sensitivity

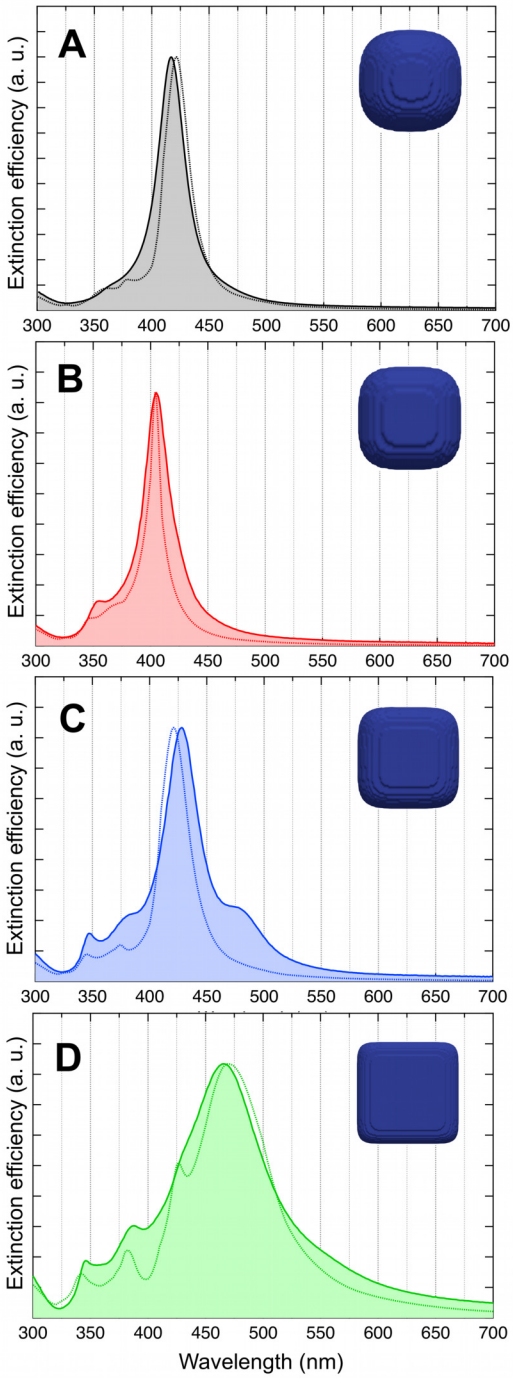

Figure 3: **Comparison of the measured and calculated extinction spectra.** Measured extinction spectra (continuous lines) are plotted along with those calculated by using the DDA method (dotted lines) for the different samples: (A) NCB(2.8), (B) NCB(3.6), (C) NCB(4.7), and (D) NCB(7.7). Toluene was used as solvent in sample NCB(2.8), whereas water was used in the other samples. All the spectra are normalized at maximum. A front view of the superellipsoid used as target in the DDA simulation is depicted in each graph.

between the dipolar and quadrupolar plasmon modes make it difficult to quantitatively compare these previous results with the present ones, where no substrate modifies the optical response of the NCBs in solution. Looking now at Figure 3C, one observes the emergence of a broad shoulder on the high wavelength side of the LSPR band, around 480 nm. Conversely, the spectra measured for samples NCB(2.8) and NCB(3.6) exhibit no similar shoulder. This latter is likely to come from the residual presence, in the colloidal solution, of nanoparticles having shapes such as truncated tetrahedra, pyramids as well as elongated particles, as seen in Figure 2C. Nanoparticles with similar shapes are also visible in TEM image of sample NCB(7.7) (Figure 2D). We would therefore expect to observe the corresponding feature on the spectrum of sample NCB(7.7), but it is not the case. This is likely due to the redshift and broadening of the main LSPR band for this sample, which prevent observing such a shoulder in the experimental extinction spectrum.

Electrodynamics calculations carried out by the DDA method

To support the interpretation of our extinction measurements, simulations were performed to calculate the extinction spectra of rounded silver NCBs with similar r parameters as those estimated for the various samples. As illustrated by the comparison made in Figure 3A–D, a pretty good agreement is found between the calculated and the measured spectra for all samples. This argues for the quality of the samples regarding their size and shape distributions and confirms that they only contain a low amount of nanoparticles with undesired shapes. This also agrees with the narrow size and shape dispersions of the NCBs observed by TEM (Figure 2A–D). As mentioned earlier, a correlation exists nevertheless between the NCB size and rounding, which makes it difficult to discern experimentally the respective effect of these two parameters on the LSPR band. The numerical simulation provides an easy way for overcoming such a limitation. Fixing the superellipsoid size to $e = 20\,\text{nm}$, extinction spectra were first calculated when varying the rounding parameter in the range $2 \leq r \leq 8$. The corresponding spectra are plotted in Figure 4A, showing the significant

increase of λ_{LSPR} with r. As illustrated by the inset of Figure 4A, in the considered range of variation in r, the dependence of the wavelength λ_{LSPR} at maximum of the major contribution is nearly linear with r. This behavior is in good qualitative agreement with what is described elsewhere[55] for similar Ag NCBs as those presented here with $r > 3$. Then, fixing the rounding parameter to $r = 3.6$, extinction spectra of Ag superellipsoids of various sizes were calculated with the size e ranging from 15 to 30 nm. As observed in Figure 4B, in contrast with the effect of the rounding parameter, the wavelength λ_{LSPR} exhibits only a slight dependence on size e. These results show the extent to which the rounding parameter can play a decisive role in the optical response of Ag NCBs, especially through the shift of the LSPR band its change can induce. The very good quantitative agreement between the experimental results and the DDA calculations shows the validity of approximating the shape of the NCBs with superellipsoids. The same approximation will be used in the following for the acoustic vibrations.

Acoustic vibrations studied by low-frequency Raman scattering

Following a previous theoretical work on the vibrations of nano-objects with rounded and sharp corners,[68] we propose to evidence experimentally the influence of the edge rounding of Ag NCBs on their acoustic vibrations. The confined acoustic eigenmodes frequencies of nanocrystals having the same shape scale as the inverse of one of their characteristic lengths. Perfect cubes have frequencies that scale as the inverse of their edge length $(1/e)$.[64,65,67] For NCBs with rounded edges, a characteristic dimension is the length of the edge of the cube it is inscribed in. However, the vibration frequencies vary with their shape, *i.e.*, the rounding of the edges. The cubic root of the volume is a better characteristic length in this context, as already demonstrated in Ref. 68. Therefore, to compare the Raman spectra from our NCBs with different edge lengths and rounding, the LFRS spectra of all samples were scaled by plotting them in Figure 5 as a function of the frequency shift, ν, multiplied by the cubic root of the related superellipsoid volume, $V^{\frac{1}{3}}$ (see Table 1). On the abscissa, the product

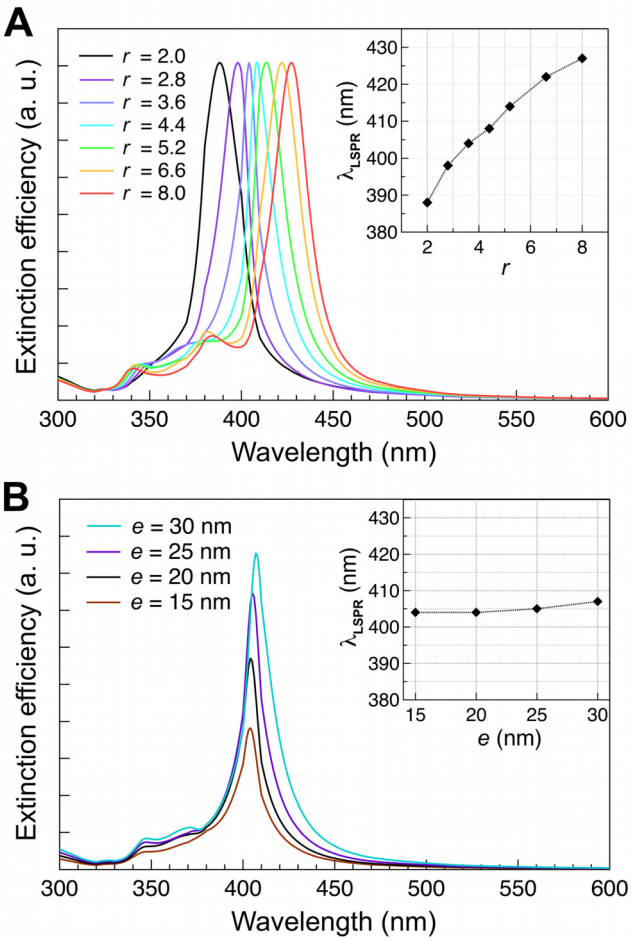

Figure 4: **Extinction spectra of Ag superellipsoids calculated using the DDA method.** From left to right in panel (A), the superellipsoid size is fixed to $e = 20\,\text{nm}$, while the rounding parameter r is progressively increased from 2.0 to 8.0. All spectra are normalized to the extinction maximum. The inset shows the variation of the wavelength at maximum, λ_{LSPR}, as a function of r. From bottom to top in panel (B), the size e is increased from 15 to 30 nm, while keeping the rounding parameter constant ($r = 3.6$). The inset shows the variation of λ_{LSPR} as a function of e.

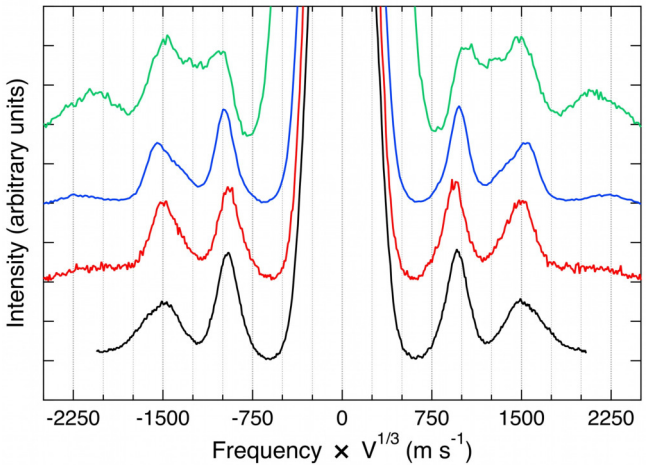

Figure 5: **Stokes/anti-Stokes LFRS spectra of Ag NCBs.** From bottom to top of the figure, the LFRS spectra were recorded from samples NCB(2.8), NCB(3.6), NCB(4.7), and NCB(7.7), respectively. The spectra are plotted as a function of the frequency shift multiplied by the characteristic NCB size, $V^{\frac{1}{3}}$. For clarity, they are also independently scaled and vertically shifted.

$\nu \times V^{\frac{1}{3}}$ is expressed in $\mathrm{m\,s^{-1}}$. As will be seen later on, when discussing the calculated normalized frequencies, for each vibration mode of NCBs, the product $\nu \times V^{1/3}$ remains roughly constant over the range of variation in r considered here. This is interesting because a given eigenmode is thus associated with a singular normalized frequency, making it much easier to assign the Raman bands as well as to compare the spectra of the various samples between them. By focusing on the signal recorded below $1800\,\mathrm{m\,s^{-1}}$, one discerns two bands whose profile is reminiscent of the Raman signal observed from monodomain quasispherical gold nanocrystals.[72] It originates mainly from the cubic structure of the lattice. This splitting of the most intense Raman peak due to the cubic lattice structure has recently been confirmed by calculating the Raman intensities.[73,74] This attests that most of the NCBs studied in this work have a single-crystal structure, as shown by HRTEM analysis. Based on previous calculations,[68] the band centered slightly below $1000\,\mathrm{m\,s^{-1}}$ is unambiguously assigned to the lowest frequency E_g mode of Ag NCBs, while the one around $1500\,\mathrm{m\,s^{-1}}$ is attributed to acoustic vibrations with the T_{2g} irreducible representation. Actually, the profile of this second band evolves from one spectrum to the other, revealing the multi-component nature

of the band. It is reasonable to assume that a moderate variation in r changes both the relative intensities and positions at maximum of these components resulting in the observed change in the profiles. The band emerging above $2000\,\mathrm{m\,s^{-1}}$ matches the lowest frequency A_{1g} vibrational mode of the NCBs and will be discussed later.

Acoustic vibrations: Numerical investigation

To go further in the interpretation of the measured LFRS signal and describe more precisely the sub-structure of the T_{2g} band and the peak at higher frequency, multipeak fitting of the spectra was performed. The Stokes and anti-Stokes parts of each spectrum were treated independently by using lorentzians. All the data resulting from the fit are detailed in SI. The spectra along with the fitting curves are plotted for the different samples in Figures S3–S6. The frequency of the lorentzians at maximum and their full width at half maximum (FWHM) are provided in Tables S3–S6. As might be expected from the change in profile of the T_{2g} band observed in Figure 5, the fit of the spectra is consistent with the existence of two underlying components. The Stokes spectrum recorded from sample NCB(4.7) is plotted together with the fitting curves in Figure 6A. From this example, one discerns the splitting of the T_{2g} band. We note that a similar splitting is observed for all the other samples. The good agreement between the frequencies and FWHM of the bands observed in the Stokes and anti-Stokes parts argues for the reliability of the multipeak fitting. Indeed, taking into account the Stokes and anti-Stokes components of the LFRS spectra serves a dual purpose: Firstly, the symmetry in both frequency shift and intensity of the bands observed between the two parts of the spectrum ensures that each band, or structured band component, arises from the inelastic light scattering by some Raman active NCB eigenvibrations. This allows to distinguish these bands from any spurious signal, such as the potential observation of secondary modes of the laser source, for instance. Secondly, for greater reliability in our measurements, the experimental frequency related to each vibration mode is evaluated as the mean value of the Stokes and anti-Stokes frequencies derived from the fit. As explained

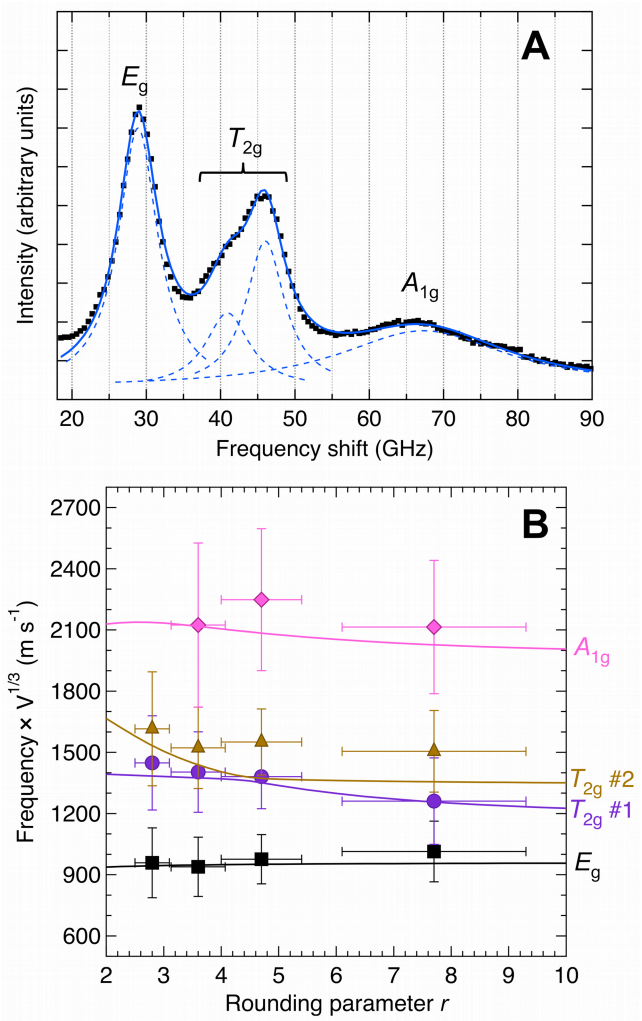

Figure 6: **Multipeak fitting of a LFRS spectrum and comparison of the measured frequencies of acoustic eigenmodes with calculated ones.** (A) Stokes LFRS spectrum of Ag NCBs recorded from the sample NCB(4.7) (black square dots) and plotted along with the lorentzians (blue dashed curves) derived from the multipeak fitting of the data. (B) Plots *versus* r of the branches corresponding to normalized frequencies ($\nu \times V^{\frac{1}{3}}$) as calculated for E_g (black curve), T_{2g} (purple and brown curves) and A_{1g} (pink curve) vibrations of Ag superellipsoids with cubic elasticity. Data points correspond to the experimental normalized frequencies (see v_{exp} in Table 2). Black squares are reported for E_g mode, purple circles and brown triangles for T_{2g} modes and pink diamonds for A_{1g} mode. The horizontal error bars correspond to the standard deviation of r while the vertical ones take into account both the errors on e and ν.

above, the normalized frequencies v_{exp}, expressed in units of $\mathrm{m\,s^{-1}}$, were then determined for each vibrational mode by multiplying the mean measured frequency by the characteristic size of the rounded NCBs (Table 1), that is :

$$v_{exp} = \frac{|\nu_{AS}| + \nu_S}{2} \times V^{\frac{1}{3}} \tag{2}$$

where ν_{AS} and ν_S are the frequency shifts at maximum of the lorentzians issued from the fit of anti-Stokes and Stokes LFRS spectra, respectively. These experimental normalized frequencies are compared in Table 2 with the ones calculated by using the Rayleigh-Ritz (RR) variational method, for the corresponding superellipsoid shape and cubic elasticity.[68]

Table 2: Comparison of the normalized frequencies, in units of $\mathrm{m\,s^{-1}}$, derived from experimental data (v_{exp}) with those calculated using the Rayleigh-Ritz variational method (v_{RR}) for the E_g, T_{2g} and A_{1g} modes of rounded Ag NCBs with cubic elasticity.

Sample	Mode	v_{exp}	v_{RR}
NCB(2.8)	E_g	958 ± 171	944
	T_{2g} (#1)	1448 ± 231	1384
	T_{2g} (#2)	1615 ± 279	1533
	A_{1g}	N/A	2137
NCB(3.6)	E_g	939 ± 145	948
	T_{2g} (#1)	1403 ± 197	1375
	T_{2g} (#2)	1522 ± 199	1438
	A_{1g}	2124 ± 402	2118
NCB(4.7)	E_g	976 ± 121	951
	T_{2g} (#1)	1381 ± 157	1351
	T_{2g} (#2)	1551 ± 162	1372
	A_{1g}	2248 ± 348	2084
NCB(7.7)	E_g	1014 ± 149	955
	T_{2g} (#1)	1261 ± 212	1257
	T_{2g} (#2)	1505 ± 200	1356
	A_{1g}	2114 ± 327	2027

The experimental and calculated values are listed in Table 2. To obtain a fair agreement between the experimental and calculated frequencies we used $\rho = 10.49\,\mathrm{g\,cm^{-3}}$, $C_{11} = 128.0 \pm 6.4\,\mathrm{GPa}$, $C_{12} = 89.4 \pm 4.5\,\mathrm{GPa}$, and $C_{44} = 46.3 \pm 0.5\,\mathrm{GPa}$. The C_{ij} coefficients differ by less than 5% from those reported for silver.[75] The Zener ratio, $Z = 2C_{44}/(C_{11} - C_{12})$, is about

2.4 ± 0.7. It is a measure of anisotropy in cubic materials. Its value is $Z = 1$ for an isotropic material and $Z = 3$ for a perfect silver crystal. The slight loss of elastic anisotropy in our samples may result from defects in the lattice structure of our NCBs. It may also come from the small amount of twinned nanocrystals.

The graph shown in Figure 6B takes us a step further in analyzing the results. Plotting the RR normalized frequencies, v_{RR}, of the different vibrational modes as a function of the rounding parameter gives rise to four branches that satisfactorily follows the experimental points, as previously revealed from the comparison in Table 2. The A_{1g} and E_g frequencies hardly depend on r. However, it is worth noting that the T_{2g} vibrations behave very differently in this r range. The substructure observed in the Raman spectra is not a real splitting because the symmetry of all the NCBs is the same (same point group) but rather the anticrossing pattern of two T_{2g} branches between $r = 4$ and $r = 5$. This pattern is related to a change in the nature of the vibrations from one side to the other of the anticrossing pattern. The vibrations of the lower frequency T_{2g} mode for $r < 4$ are similar to those of the higher frequency T_{2g} mode for $r > 5$, and reciprocally. The deformation associated with the two modes are illustrated in Figure 7 (see also the animations available in SI). They originate from the fundamental spheroidal $\ell = 2$ (quadrupolar) and torsional $\ell = 3$ vibrations of the isotropic sphere. The first one is at lower frequency for a sphere and higher frequency for a cube. Note that the observation of such an anticrossing is quite rare. It has been investigated for core-shell nanoparticles with time-resolved pump-probe transient absorption measurements when varying the thickness of the shell[22,41] but, to the best of our knowledge, it has not been reported for simple nanoparticles. Another difference can be spotted in the FWHM of the T_{2g} bands obtained from the multipeak fitting of the LFRS spectra (Tables S3–S6 in SI), which we relate to the change in nature of the vibrations. For sample NCB(2.8), the FWHM of the E_g band is close to that of the lower frequency T_{2g} mode. However, it is closer to that of the higher frequency T_{2g} mode for the other samples with larger rounding parameter r. We tentatively assign this behavior to the different inhomogeneous broadening resulting

from the dependence of the frequency of these modes on the exact shape of the nanocrystals. The "quadrupolar-like" modes are quite robust with respect to the shape of the nanocrystals and vary mostly as $V^{\frac{1}{3}}$, as explained above. Therefore, the inhomogeneous broadening of this peak is mainly related to the volume distribution. Torsional-like vibrations are more sensitive to the actual shape because the motions are similar to rotations and the torques involved depend on the distance from the center. Scattering by torsional-like modes is very unusual but in the present case, none of the two T_{2g} modes is purely torsional due to the anti-crossing. We can also note that a torsional vibration does not change the shape of a sphere, but it does change the shape of a cube. This difference may activate the surface scattering mechanism in non-spherical NCBs which does not apply for torsional vibrations in isotropic spheres. It originates from the strong sensitivity of the localized surface plasmon resonance to the shape of the nanoparticles.

The peak at higher frequency is assigned to the lowest frequency A_{1g} mode. Note that this mode is not the "breathing-like" mode whose normalized frequency is above $2600\,\mathrm{m\,s^{-1}}$. It corresponds to the spheroidal $\ell = 4$ vibration of an isotropic sphere and is Raman inactive in that case. This strong selection rule does not hold anymore when the symmetry becomes cubic. Still, this Raman peak is not observed for a sphere made of cubic material.[72] In the present case, its intensity increases as the shape evolves toward a cube. In addition, it is significantly larger for NCB(7.7). This quick evolution of the intensities of this additional T_{2g} peak and the A_{1g} peak between NCB(4.7) and NCB(7.7) is unexpected. We assign it to the larger size and the arrangement of the NCBs in NCB(7.7). Indeed, the NCBs seem to be much closer for this sample in Figure 2 than for the other ones. As a matter of fact, whatever the sample considered in this work, the edge-to-edge distance s between NCBs, after deposition on a silicon substrate, mainly depends on surface chemistry and hardly fluctuates from sample to sample. At nearly fixed distance s, the relative inter-nanoparticle distance s/e logically decreases for increasing NCB edge length e, being lowest for the sample NCB(7.7). As previously reported for gold nanorods, inter-nanoparticle electromagnetic interactions

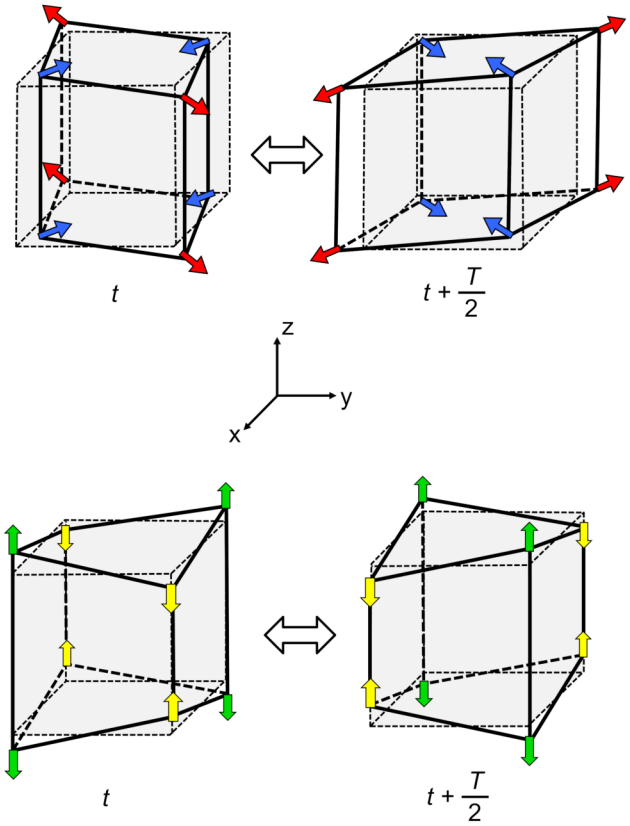

Figure 7: **Illustration of the two T_{2g} modes for a cube.** The "quadrupolar-like" mode depicted at the top, involves compression (blue arrows) and expansion (red arrows) motions along the diagonals in the xy plane while the "torsional $\ell = 3$"-like mode, at the bottom, involves compression (yellow arrows) and expansion (green arrows) motions of the edges along the z direction. These modes are represented at two instants t and $t + \frac{T}{2}$ that differ by half of their period T, when the displacement amplitude is maximum. In each case, the cube at rest is shown in light gray with dotted lines.

increase when the ratio s/D of the distance between the nanoparticles to their size decreases. As a result, the usual Raman selection rules are relaxed and inelastic scattering of light becomes possible by other vibrations, such as the spheroidal ones with $\ell > 2$ for isotropic spheres.[36]

Conclusion

Silver nanocubes of various sizes were synthesized by chemical routes. We obtained different batches of nanocubes characterized by a small dispersion both in size and shape. The actual nanocube shapes with more or less rounded edges are conveniently modeled by superellipsoids. Extinction measurements supported by DDA calculations demonstrate the significant impact of edge rounding on the localized surface plasmon resonance, with a significant redshift in its main component as the edges become sharper. The shift of this band induced by a modest variation in the rounding parameter is much more pronounced than the one produced by a change in the nanocube size at fixed rounding parameter. Using low-frequency Raman scattering spectroscopy, edge rounding is also demonstrated to have a significant effect on the acoustic vibrations of nanocubes through the rounding dependent $V^{\frac{1}{3}}$ scaling but also through the T_{2g} band substructure. The variations of the frequencies and FWHM as a function of the rounding parameter regarding both T_{2g} modes suggest that these modes change in nature, in agreement with what is expected from the calculated anti-crossing pattern. In addition, the Raman spectra are shown to also depend on the arrangement of the nanocubes. Scattering by additional modes occurs when the inter-nanoparticle electromagnetic interaction increases, *i.e.*, for decreasing values of the ratio of the inter-nanocube distance to the size of the nanocube. Extension of this work to analyze the dependence of the inelastic light scattering signal recorded from rounded nanocubes upon change of the excitation wavelength will be of great interest for studying the acousto-plasmonic interaction in such nanoobjects. Experimental data on this subject would support in particular the recent development of nu-

merical models to calculate the Raman intensity[73,74] for non-spherical elastically anisotropic nanoparticles.

Methods

Syntheses of rounded Ag NCBs

To carry out the syntheses described below, all the chemicals were used as received: Silver nitrate (Sigma-Aldrich, $\geq$ 99%), sodium borohydride (Acros Organics Chemicals, $\geq$ 96%), cetyltrimethylammonium chloride (TCI, $\geq$ 95%), silver trifluoroacetate (Sigma-Aldrich, $\geq$ 98%), L-ascorbic acid (Alfa Aesar, $\geq$ 98%), dichlorobenze (Sigma-Aldrich, 99%), Oleylamine (Sigma-Aldrich, $\geq$ 80%). Solutions were made with ultrapure water (18.2 MΩ cm) and fresh daily prepared.

Synthesis of roundest Ag NCBs related to sample NCB(2.8) (following the protocol described in Ref. 69): 0.06 mmol of CF_3COOAg were added to 2 mL of oleylamine in a round bottom flask and were stirred at 30°C for at least 30 min to ensure dissolution of the Ag precursor. Then, 100 mL of dichlorobenzene were added and the temperature was raised to 165°C at a rate of 300°C/h, and was kept at this temperature with stirring during 12 h under air atmosphere. The solution was then cooled to room temperature before being washed with a toluene:acetone ratio of 1:1 and centrifuged at 2000 rpm for 5 min. The supernatant was removed and the precipitate was dispersed in toluene. This step was repeated once and Ag NCBs were finally redispersed in toluene and concentrated for TEM analysis and LFRS measurements.

Synthesis of Ag NCBs with higher rounding paramaters ($r > 3$): A seed mediated protocol published elsewhere was used.[70] The latter is based on the preparation of two solutions, *i.e.* the seed and growth solutions, as follows. For the seed solution, 25 μL of

$AgNO_3$ (0.1 M) were added to 9.5 mL of a CTAC solution (0.5 mM) under slow stirring in a 20 mL glass vial. After 5 min, 450 μL of freshly made $NaBH_4$ (0.02 M) was added in one stroke under strong stirring. The solution immediately turned yellow. The seeds solution was aged at 30°C for 30 min with stirring. The seeds solution was then wrapped in aluminum foil to be aged for 10 days at room temperature without disturbance. For the growth solution, 40 mg of CTAC, 100 μL of aqueous CF_3COOAg (0.1 M) and 1000, 300 or 50 μL of aged seeds were added to a 20 mL vial for samples NCB(3.6), NCB(4.7), and NCB(7.7), respectively. MiliQ water was added, so that the total volume in the vial is 9 mL. The growth solution was set in water bath at 60°C for 20 min, while stirring. Then, 1 mL of ascorbic acid (0.1 M) was added. After 90 min, the reaction was stopped and the Ag NCBs were centrifuged (at 22000 g for NCB(3.6), 6000 g for NCB(4.7), and 2000 g for NCB(7.7)) twice for 15 min and redispersed in CTAC (1 mM). After the second washing step, the Ag NCBs were redispersed in a smaller volume of water to concentrate them before their characterization by TEM imaging and LFRS measurements. This second protocol allows synthesizing Ag nanocrystals whose final size and shape depend on the relative amount of seeds and chloride ions in solution. By decreasing the concentration of seeds at fixed concentration of Cl^-, the size of the formed nanocrystals increases while their shape evolves towards that of NCBs with sharp edges.[76] This might explain the simultaneous increase in both e and r that is observed for NCBs issued from samples NCB(3.6), NCB(4.7), and NCB(7.7), successively.

TEM and HRTEM analysis

To estimate experimentally both the NCB size and the mean rounding parameter, imaging of the synthesized NCBs was performed by using JEOL 1011 and JEOL 2011 microscopes for conventional TEM and HRTEM, respectively. The samples were prepared by depositing 2 μL of colloidal solution onto a copper grid covered by an amorphous carbon film. The size distributions were determined using the NIH ImageJ software over a batch of hundreds of particles. In practice, the NCB sizes were indirectly estimated by means of the superellipse

surface provided by numerical analysis of the TEM images (see Figure S2 in SI).

Electrodynamics calculations by the DDA method

The calculations were carried out by using the Discrete Dipole Approximation (DDA) method [77] applied in the DDSCAT 7.3 freely available open-source software package. [78] The DDA method is well suited and commonly used for calculating the absorption coefficients of metal particles having irregular shapes. [3,4,79] The dielectric function of silver published by Johnson and Christy [80] was chosen over other data sources because it appears to describe more reliably perfect crystalline nanoparticles. [60] This dielectric function was nevertheless size corrected within the frame of the Drude model based on a geometric approach. [81] For all calculations, the interdipole distance d was fixed to 0.5 nm and the superellipsoid target was created using the in-built shape generator SUPELLIPS recently implemented in the DDSCAT 7.3.3 distribution. [78] The refractive index of the surrounding medium was set to that of water ($n = 1.33$), except for sample NCB(2.8), for which it was set to the one of toluene ($n = 1.49$). The other fitting parameters involved in the program to model each superellipsoid are quoted in Table S2 in SI.

Low-frequency Raman scattering measurements

LFRS measurements were performed using a TFP-2 HC high contrast spectrometer. This instrument is a six-pass vernier tandem Fabry-Pérot interferometer [82] with a typical contrast of more than 10^{15} and a finesse of 120. It is primarily designed to perform inelastic light scattering measurements at ultra-low frequency, and is therefore perfectly suited to studying the acoustic vibrations of nano-objects. The scattered light was collected in backscattering configuration with a $\times 100$ microscope objective. The excitation source was a frequency doubled Nd-YAG solid state laser emitting at 532.2 nm and the H10682-210 multi-pixel photon counting module from Hamamatsu was used for the detection. For these measurements, Ag NCBs were deposited by drop-casting onto a silicon wafer using 5 μL of concentrated

solutions.

Rayleigh-Ritz variational method

RR calculations were carried out using the xyz algorithm introduced by Visscher *et al.*[83] and applied to superellipsoids made of cubic silver. The lengths and rounding parameters along x, y and z are identical and the 100 directions of the cubic lattice structure of silver are along x, y and z resulting in nanocrystals having the cubic symmetry (point group O_h). This symmetry was taken into account to speed up the calculations by considering the eigenvibrations of each irreducible representation separately. These calculations can be reproduced and visualized online.[84]

Acknowledgement

The authors thank Dr. N. Goubet from Sorbonne Université (MONARIS, UMR 8233 CNRS-SU) for imaging nanocubes by HRTEM. HP thanks Dr. A. Girard from the same lab for his help in setting up the tandem Fabry-Pérot interferometer used in this work. LS acknowledges support by the EIPHI Graduate School (Contract ANR-17-EURE-0002).

Supporting Information Available

The following files are available free of charge.

- Ag-nanocubes-SI.pdf: Details on the calculation of the superellipsoid volume and the superellipse surface area. Table quoting the fitting parameters used in DDA simulation. LFRS spectra recorded for all the samples and data resulting from their multipeak fitting summarized in separate tables.

- Eg.mp4: Animation showing the motions of a cube (superellipsoid with $r = 100$) in the E_g mode.

- T2g-1.mp4: Animation showing the motions of a cube (superellipsoid with $r = 100$) in the "torsional $\ell = 3$"-like T_{2g} mode.

- T2g-2.mp4: Animation showing the motions of a cube (superellipsoid with $r = 100$) in the "quadrupolar-like" T_{2g} mode.

- A1g.mp4: Animation showing the motions of a cube (superellipsoid with $r = 100$) in the A_{1g} mode.

References

1. Kelly, K. L.; Coronado, E.; Zhao, L. L.; Schatz, G. C. The Optical Properties of Metal Nanoparticles: The Influence of Size, Shape, and Dielectric Environment. *J. Phys. Chem. B* **2003**, *107*, 668–677.

2. Lee, K.-S.; El-Sayed, M. A. Gold and Silver Nanoparticles in Sensing and Imaging: Sensitivity of Plasmon Response to Size, Shape, and Metal Composition. *J. Phys. Chem. B* **2006**, *110*, 19220–19225.

3. Wiley, B. J.; Im, S. H.; Li, Z.-Y.; McLellan, J.; Siekkinen, A.; Xia, Y. Maneuvering the Surface Plasmon Resonance of Silver Nanostructures through Shape-Controlled Synthesis. *J. Phys. Chem. B* **2006**, *110*, 15666–15675.

4. Noguez, C. Surface Plasmons on Metal Nanoparticles: The Influence of Shape and Physical Environment. *J. Phys. Chem. C* **2007**, *111*, 3806–3819.

5. Sau, T. K.; Rogach, A. L.; Jäckel, F.; Klar, T. A.; Feldmann, J. Properties and Applications of Colloidal Nonspherical Noble Metal Nanoparticles. *Adv. Mater.* **2010**, *22*, 1805–1825.

6. Mejía-Salazar, J. R.; Oliveira, O. N. J. Plasmonic Biosensing. *Chem. Rev.* **2018**, *118*, 10617–10625.

7. Jauffred, L.; Samadi, A.; Klingberg, H.; Bendix, P. M.; Oddershede, L. B. Plasmonic Heating of Nanostructures. *Chem. Rev.* **2019**, *119*, 8087–8130.

8. Chapus, L.; Aubertin, P.; Joiret, S.; Lucas, I. T.; Maisonhaute, E.; Courty, A. Tunable SERS Platforms from Small Nanoparticle 3D Superlattices: A Comparison between Gold, Silver, and Copper. *Chem. Phys. Chem.* **2017**, *18*, 3066–3075.

9. Zong, C.; Xu, M.; Xu, L.-J.; Wei, T.; Ma, X.; Zheng, X.-S.; Hu, R.; Ren, B. Surface-Enhanced Raman Spectroscopy for Bioanalysis: Reliability and Challenges. *Chem. Rev.* **2018**, *118*, 4946–4980.

10. Muskens, O. L.; Bachelier, G.; Del Fatti, N.; Vallée, F.; Brioude, A.; Jiang, X.; Pileni, M.-P. Quantitative Absorption Spectroscopy of a Single Gold Nanorod. *J. Phys. Chem. C* **2008**, *112*, 8917–8921.

11. Henry, A.-I.; Bingham, J. M.; Ringe, E.; Marks, L. D.; Schatz, G. C.; Van Duyne, R. P. Correlated Structure and Optical Property Studies of Plasmonic Nanoparticles. *J. Phys. Chem. C* **2011**, *115*, 9291–9305.

12. Crut, A.; Maioli, P.; Del Fatti, N.; Vallée, F. Optical Absorption and Scattering Spectroscopies of Single Nano-Objects. *Chem. Soc. Rev.* **2014**, *43*, 3921–3956.

13. Duval, E.; Boukenter, A.; Champagnon, B. Vibration Eigenmodes and Size of Microcrystallites in Glass: Observation by Very-Low-Frequency Raman Scattering. *Phys. Rev. Lett.* **1986**, *56*, 2052–2055.

14. Del Fatti, N.; Voisin, C.; Chevy, F.; Vallée, F.; Flytzanis, C. Coherent Acoustic Mode Oscillation and Damping in Silver Nanoparticles. *J. Chem. Phys.* **1999**, *110*, 11484–11487.

15. Hodak, J. H.; Henglein, A.; Hartland, G. V. Size Dependent Properties of Au Particles:

Coherent Excitation and Dephasing of Acoustic Vibrational Modes. *J. Chem. Phys.* **1999**, *111*, 8613–8621.

16. Hu, M.; Wang, X.; Hartland, G. V.; Mulvaney, P.; Juste, J. P.; Sader, J. E. Vibrational Response of Nanorods to Ultrafast Laser Induced Heating: Theoretical and Experimental Analysis. *J. Am. Chem. Soc.* **2003**, *125*, 14925–14933.

17. Crut, A.; Maioli, P.; Fatti, N. D.; Vallée, F. Anisotropy Effects on the Time-Resolved Spectroscopy of the Acoustic Vibrations of Nanoobjects. *Phys. Chem. Chem. Phys.* **2009**, *11*, 5882–5888.

18. Pan, H. H.; Wang, Z. K.; Lim, H. S.; Ng, S. C.; Zhang, V. L.; Kuok, M. H.; Tran, T. T.; Lu, X. M. Hypersonic Confined Eigenvibrations of Gold Nano-Octahedra. *Appl. Phys. Lett.* **2011**, *98*, 133123.

19. Portalès, H.; Saviot, L.; Duval, E.; Gaudry, M.; Cottancin, E.; Lermé, J.; Pellarin, M.; Broyer, M.; Prèvel, B.; Treilleux, M. Resonance and Composition Effects on the Raman Scattering from Silver-Gold Alloy Clusters. *Eur. Phys. J. D* **2001**, *16*, 197–200.

20. Zijlstra, P.; Tchebotareva, A. L.; Chon, J. W. M.; Gu, M.; Orrit, M. Acoustic Oscillations and Elastic Moduli of Single Gold Nanorods. *Nano Lett.* **2008**, *8*, 3493–3497.

21. Yu, K.; Sader, J. E.; Zijlstra, P.; Hong, M.; Xu, Q.-H.; Orrit, M. Probing Silver Deposition on Single Gold Nanorods by Their Acoustic Vibrations. *Nano Lett.* **2014**, *14*, 915–922.

22. Mongin, D.; Juvé, V.; Maioli, P.; Crut, A.; Del Fatti, N.; Vallée, F.; Sánchez-Iglesias, A.; Pastoriza-Santos, I.; Liz-Marzán, L. M. Acoustic Vibrations of Metal-Dielectric Core–Shell Nanoparticles. *Nano Lett.* **2011**, *11*, 3016–3021.

23. Voisin, C.; Christofilos, D.; Del Fatti, N.; Vallée, F. Environment Effect on the Acoustic Vibration of Metal Nanoparticles. *Physica B* **2002**, *316-317*, 89–94.

24. Pelton, M.; Sader, J. E.; Burgin, J.; Liu, M.; Guyot-Sionnest, P.; Gosztola, D. Damping of Acoustic Vibrations in Gold Nanoparticles. *Nature Nanotech.* **2009**, *4*, 492–495.

25. Hartland, G. V. Optical Studies of Dynamics in Noble Metal Nanostructures. *Chem. Rev.* **2011**, *111*, 3858–3887.

26. Yu, K.; Zijlstra, P.; Sader, J. E.; Xu, Q.-H.; Orrit, M. Damping of Acoustic Vibrations of Immobilized Single Gold Nanorods in Different Environments. *Nano Lett.* **2013**, *13*, 2710–2716.

27. Bachelier, G.; Margueritat, J.; Mlayah, A.; Gonzalo, J.; Afonso, C. N. Size Dispersion Effects on the Low-Frequency Raman Scattering of Quasispherical Silver Nanoparticles: Experiment and Theory. *Phys. Rev. B* **2007**, *76*, 235419.

28. Petrova, H.; Perez-Juste, J.; Zhang, Z.; Zhang, J.; Kosel, T.; Hartland, G. V. Crystal Structure Dependence of the Elastic Constants of Gold Nanorods. *J. Mater. Chem.* **2006**, *16*, 3957–3963.

29. Juvé, V.; Crut, A.; Maioli, P.; Pellarin, M.; Broyer, M.; Del Fatti, N.; Vallée, F. Probing Elasticity at the Nanoscale: Terahertz Acoustic Vibration of Small Metal Nanoparticles. *Nano Lett.* **2010**, *10*, 1853–1858.

30. Stephanidis, B.; Adichtchev, S.; Etienne, S.; Migot, S.; Duval, E.; Mermet, A. Vibrations of Nanoparticles: From Nanospheres to FCC Cuboctahedra. *Phys. Rev. B* **2007**, *76*, 121404.

31. Portalès, H.; Goubet, N.; Saviot, L.; Adichtchev, S.; Murray, D. B.; Mermet, A.; Duval, E.; Pileni, M.-P. Probing Atomic Ordering and Multiple Twinning in Metal Nanocrystals through Their Vibrations. *Proc. Natl. Acad. of Sci. U.S.A.* **2008**, *105*, 14784–14789.

32. Portalès, H.; Goubet, N.; Saviot, L.; Yang, P.; Sirotkin, S.; Duval, E.; Mermet, A.; Pileni, M.-P. Crystallinity Dependence of the Plasmon Resonant Raman Scattering by Anisotropic Gold Nanocrystals. *ACS Nano* **2010**, *4*, 3489–3497.

33. Ostovar, B.; Su, M.-N.; Renard, D.; Clark, B. D.; Dongare, P. D.; Dutta, C.; Gross, N.; Sader, J. E.; Landes, C. F.; Chang, W.-S. *et al.* Acoustic Vibrations of Al Nanocrystals: Size, Shape, and Crystallinity Revealed by Single-Particle Transient Extinction Spectroscopy. *J. Phys. Chem. A* **2020**, *124*, 3924–3934.

34. Major, T. A.; Crut, A.; Gao, B.; Lo, S. S.; Del Fatti, N.; Vallée, F.; Hartland, G. V. Damping of the Acoustic Vibrations of a Suspended Gold Nanowire in Air and Water Environments. *Phys. Chem. Chem. Phys.* **2013**, *15*, 4169–4176.

35. Girard, A.; Gehan, H.; Mermet, A.; Bonnet, C.; Lermé, J.; Berthelot, A.; Cottancin, E.; Crut, A.; Margueritat, J. Acoustic Mode Hybridization in a Single Dimer of Gold Nanoparticles. *Nano Lett.* **2018**, *18*, 3800–3806.

36. Girard, A.; Lermé, J.; Gehan, H.; Mermet, A.; Bonnet, C.; Cottancin, E.; Crut, A.; Margueritat, J. Inelastic Light Scattering by Multiple Vibrational Modes in Individual Gold Nanodimers. *J. Phys. Chem. C* **2019**, *123*, 14834–14841.

37. Lermé, J.; Margueritat, J.; Crut, A. Vibrations of Dimers of Mechanically Coupled Nanostructures: Analytical and Numerical Modeling. *J. Phys. Chem. C* **2021**, *125*, 8339–8348.

38. Noual, A.; Kang, E.; Maji, T.; Gkikas, M.; Djafari-Rouhani, B.; Fytas, G. Optomechanic Coupling in Ag Polymer Nanocomposite Films. *J. Phys. Chem. C* **2021**, *125*, 14854–14864.

39. Courty, A.; Mermet, A.; Albouy, P. A.; Duval, E.; Pileni, M. P. Vibrational Coherence of Self-Organized Silver Nanocrystals in F.C.C. Supra-Crystals. *Nat. Mater.* **2005**, *4*, 395–398.

40. Portalès, H.; Goubet, N.; Casale, S.; Xu, X. Z.; Ariane, M.; Mermet, A.; Margueritat, J.; Saviot, L. Inelastic Light Scattering by Long Narrow Gold Nanocrystals: When Size, Shape, Crystallinity, and Assembly Matter. *ACS Nano* **2020**, *14*, 4395–4404.

41. Dacosta Fernandes, B.; Vilar-Vidal, N.; Baida, H.; Massé, P.; Oberlé, J.; Ravaine, S.; Tréguer-Delapierre, M.; Saviot, L.; Langot, P.; Burgin, J. Acoustic Vibrations of Core–Shell Nanospheres: Probing the Mechanical Contact at the Metal–Dielectric Interface. *J. Phys. Chem. C* **2018**, *122*, 9127–9133.

42. Saviot, L.; Mermet, A.; Duval, E. In *Nanoparticles and Quantum Dots*; Sattler, K. D., Ed.; Handbook of Nanophysics; CRC Press: Boca Raton, FL, USA, 2010; Chapter 11, pp 11.1–11.17.

43. Crut, A.; Maioli, P.; Del Fatti, N.; Vallée, F. Acoustic Vibrations of Metal Nano-Objects: Time-Domain Investigations. *Phys. Rep.* **2015**, *549*, 1–43.

44. Hodak, J. H.; Henglein, A.; Hartland, G. V. Photophysics of Nanometer Sized Metal Particles: Electron–Phonon Coupling and Coherent Excitation of Breathing Vibrational Modes. *J. Phys. Chem. B* **2000**, *104*, 9954–9965.

45. Voisin, C.; Del Fatti, N.; Christofilos, D.; Vallée, F. Ultrafast Electron Dynamics and Optical Nonlinearities in Metal Nanoparticles. *J. Phys. Chem. B* **2001**, *105*, 2264–2280.

46. Duval, E. Far-Infrared and Raman Vibrational Transitions of a Solid Sphere: Selection Rules. *Phys. Rev. B* **1992**, *46*, 5795–5797.

47. Herzberg, Z. In *Molecular Spectra and Molecular Structure: Spectra of Diatomic Molecules*; 2nd ed.; Nostrand, V., Ed.; D. Van Nostrand Company, Inc.: New York, 1945; Vol. 1.

48. Weitz, D. A.; Gramila, T. J.; Genack, A. Z.; Gersten, J. I. Anomalous Low-Frequency

Raman Scattering from Rough Metal Surfaces and the Origin of Surface-Enhanced Raman Scattering. *Phys. Rev. Lett.* **1980**, *45*, 355–358.

49. Palpant, B.; Portalès, H.; Saviot, L.; Lermé, J.; Prével, B.; Pellarin, M.; Duval, E.; Perez, A.; Broyer, M. Quadrupolar Vibrational Mode of Silver Clusters from Plasmon-Assisted Raman Scattering. *Phys. Rev. B* **1999**, *60*, 17107–17111.

50. Portalès, H.; Saviot, L.; Duval, E.; Fujii, M.; Hayashi, S.; Del Fatti, N.; Vallée, F. Resonant Raman Scattering by Breathing Modes of Metal Nanoparticles. *J. Chem. Phys.* **2001**, *115*, 3444–3447.

51. Bachelier, G.; Mlayah, A. Surface Plasmon Mediated Raman Scattering in Metal Nanoparticles. *Phys. Rev. B* **2004**, *69*, 205408.

52. Girard, A.; Lermé, J.; Gehan, H.; Margueritat, J.; Mermet, A. Mechanisms of Resonant Low Frequency Raman Scattering from Metallic Nanoparticle Lamb Modes. *J. Chem. Phys.* **2017**, *146*, 194201.

53. Park, J.-E.; Lee, Y.; Nam, J.-M. Precisely Shaped, Uniformly Formed Gold Nanocubes with Ultrahigh Reproducibility in Single-Particle Scattering and Surface-Enhanced Raman Scattering. *Nano Lett.* **2018**, *18*, 6475–6482.

54. Mann, M. E.; Yadav, P.; Kim, S. Colloidal Plasmonic Nanocubes As Capacitor Building Blocks for Multidimensional Optical Metamaterials: A Review. *ACS Appl. Nano Mater.* **2021**, *4*, 9976–9984.

55. Bronchy, M.; Roach, L.; Mendizabal, L.; Feautrier, C.; Durand, E.; Heintz, J.-M.; Duguet, E.; Tréguer-Delapierre, M. Improved Low Temperature Sinter Bonding Using Silver Nanocube Superlattices. *J. Phys. Chem. C* **2022**, *126*, 1644–1650.

56. Pawlik, V.; Zhou, S.; Zhou, S.; Qin, D.; Xia, Y. Silver Nanocubes: From Serendipity to

Mechanistic Understanding, Rational Synthesis, and Niche Applications. *Chem. Mater.* **2023**, *35*, 3427–3449.

57. Alpay, D.; Peng, L.; Marks, L. D. Are Nanoparticle Corners Round? *J. Phys. Chem. C* **2015**, *119*, 21018–21023.

58. Clark, B. D.; Jacobson, C. R.; Lou, M.; Renard, D.; Wu, G.; Bursi, L.; Ali, A. S.; Swearer, D. F.; Tsai, A.-L.; Nordlander, P. *et al.* Aluminum Nanocubes Have Sharp Corners. *ACS Nano* **2019**, *13*, 9682–9691.

59. McLellan, J. M.; Siekkinen, A.; Chen, J.; Xia, Y. Comparison of the Surface-Enhanced Raman Scattering on Sharp and Truncated Silver Nanocubes. *Chem. Phys. Lett.* **2006**, *427*, 122–126.

60. McMahon, J. M.; Wang, Y.; Sherry, L. J.; Van Duyne, R. P.; Marks, L. D.; Gray, S. K.; Schatz, G. C. Correlating the Structure, Optical Spectra, and Electrodynamics of Single Silver Nanocubes. *J. Phys. Chem. C* **2009**, *113*, 2731–2735.

61. Grillet, N.; Manchon, D.; Bertorelle, F.; Bonnet, C.; Broyer, M.; Cottancin, E.; Lermé, J.; Hillenkamp, M.; Pellarin, M. Plasmon Coupling in Silver Nanocube Dimers: Resonance Splitting Induced by Edge Rounding. *ACS Nano* **2011**, *5*, 9450–9462.

62. Pellarin, M.; Ramade, J.; Rye, J. M.; Bonnet, C.; Broyer, M.; Lebeault, M.-A.; Lermé, J.; Marguet, S.; Navarro, J. R.; Cottancin, E. Fano Transparency in Rounded Nanocube Dimers Induced by Gap Plasmon Coupling. *ACS Nano* **2016**, *10*, 11266–11279.

63. Timm, M. M.; Saviot, L.; Crut, A.; Blanchard, N.; Roiban, L.; Masenelli-Varlot, K.; Joly-Pottuz, L.; Margueritat, J. Study of Single Gold Nanocrystals by Inelastic Light Scattering Spectroscopy. *J. Phys. Chem. C* **2022**, *126*, 3606–3613.

64. Li, Y.; Lim, H. S.; Ng, S. C.; Kuok, M. H.; Ge, M. Y.; Jiang, J. Z. Brillouin Study of Acoustic Phonon Confinement in GeO_2 Nanocubes. *Appl. Phys. Lett.* **2007**, *91*, 093116.

65. Petrova, H.; Lin, C.-H.; de Liejer, S.; Hu, M.; McLellan, J. M.; Siekkinen, A. R.; Wiley, B. J.; Marquez, M.; Xia, Y.; Sader, J. E. *et al.* Time-Resolved Spectroscopy of Silver Nanocubes: Observation and Assignment of Coherently Excited Vibrational Modes. *J. Chem. Phys.* **2007**, *126*, 094709.

66. Staleva, H.; Hartland, G. V. Transient Absorption Studies of Single Silver Nanocubes. *J. Phys. Chem. C* **2008**, *112*, 7535–7539.

67. Sun, J.; Wang, Z.; Lim, H.; Zhang, V.; Ng, S.; Kuok, M.; Zhang, W.; Firdoz, S.; Lu, X. Brillouin Study of Confined Eigenvibrations of Silver Nanocubes. *Sol. State Comm.* **2012**, *152*, 501–503.

68. Saviot, L. Free Vibrations of Anisotropic Nano-Objects with Rounded or Sharp Corners. *Nanomaterials* **2021**, *11*, 1838.

69. Polavarapu, L.; Liz-Marzán, L. M. Growth and Galvanic Replacement of Silver Nanocubes in Organic Media. *Nanoscale* **2013**, *5*, 4355–4361.

70. Lin, Z.-W.; Tsao, Y.-C.; Yang, M.-Y.; Huang, M. H. Seed-Mediated Growth of Silver Nanocubes in Aqueous Solution with Tunable Size and Their Conversion to Au Nanocages with Efficient Photothermal Property. *Chem. Eur. J.* **2016**, *22*, 2326–2332.

71. Cherqui, C.; Li, G.; Busche, J. A.; Quillin, S. C.; Camden, J. P.; Masiello, D. J. Multipolar Nanocube Plasmon Mode-Mixing in Finite Substrates. *J. Phys. Chem. Lett.* **2018**, *9*, 504–512.

72. Portalès, H.; Goubet, N.; Sirotkin, S.; Duval, E.; Mermet, A.; Albouy, P.-A.; Pileni, M.-P. Crystallinity Segregation upon Selective Self-Assembling of Gold Colloidal Single Nanocrystals. *Nano Lett.* **2012**, *12*, 5292–5298.

73. Montaño Priede, J. L.; Mlayah, A.; Large, N. Raman Energy Density in the Context of Acoustoplasmonics. *Phys. Rev. B* **2022**, *106*, 165425.

74. Vasileiadis, T.; Noual, A.; Wang, Y.; Graczykowski, B.; Djafari-Rouhani, B.; Yang, S.; Fytas, G. Optomechanical Hot-Spots in Metallic Nanorod–Polymer Nanocomposites. *ACS Nano* **2022**, *16*, 20419–20429.

75. Neighbours, J. R.; Alers, G. A. Elastic Constants of Silver and Gold. *Phys. Rev.* **1958**, *111*, 707–712.

76. Chen, Z.; Balankura, T.; Fichthorn, K. A.; Rioux, R. M. Revisiting the Polyol Synthesis of Silver Nanostructures: Role of Chloride in Nanocube Formation. *ACS Nano* **2019**, *13*, 1849–1860.

77. Draine, B. T.; Flatau, P. J. Discrete-Dipole Approximation for Scattering Calculations. *J. Opt. Soc. Am. A* **1994**, *11*, 1491–1499.

78. Draine, B. T.; Flatau, P. J. DDSCAT 7.3. `https://www.astro.princeton.edu/~draine/DDSCAT.7.3.html`, (Accessed July 27, 2023).

79. Yang, P.; Portalès, H.; Pileni, M.-P. Dependence of the Localized Surface Plasmon Resonance of Noble Metal Quasispherical Nanoparticles on Their Crystallinity-Related Morphologies. *J. Chem. Phys.* **2011**, *134*, 024507.

80. Johnson, P. B.; Christy, R. W. Optical Constants of the Noble Metals. *Phys. Rev. B* **1972**, *6*, 4370–4379.

81. Coronado, E. A.; Schatz, G. C. Surface Plasmon Broadening for Arbitrary Shape Nanoparticles: A Geometrical Probability Approach. *J. Chem. Phys.* **2003**, *119*, 3926–3934.

82. Lindsay, S. M.; Anderson, M. W.; Sandercock, J. R. Construction and Alignment of a High Performance Multipass Vernier Tandem Fabry-Perot Interferometer. *Rev. Sci. Instrum.* **1981**, *52*, 1478–1486.

83. Visscher, W. M.; Migliori, A.; Bell, T. M.; Reinert, R. A. On the Normal Modes of Free Vibration of Inhomogeneous and Anisotropic Elastic Objects. *J. Acoust. Soc. Am.* **1991**, *90*, 2154–2162.

84. Saviot, L. Vibrations of Anisotropic Nano-Objects. `https://saviot.cnrs.fr/rus/index.en.html`, (Accessed July 27, 2023).

Graphical TOC Entry